USING THE SHALLOW STRAIN TENSOR TO CHARACTERIZE DEEP GEOLOGIC RESERVOIRS

Authors: Lawrence C. Murdoch*[1], Scott DeWolf[1], Leonid N. Germanovich[1], Stephen Moysey[2], Alex Hanna[3], Soheil Roudini[1], Robert Moak[1]

Affiliations:

1. Environmental Engineering and Earth Science Department. Clemson University, Clemson, South Carolina, USA.
2. Eastern Carolina University, Greenville, North Carolina.
3. Pacific Northwest National Laboratory

*Corresponding author: lmurdoc@clemson.edu

KEY POINTS

- The strain tensor at shallow depths responds to pumping in underlying reservoirs or aquifers
- The shallow strain tensor can be measured and analyzed to estimate subsurface properties or characterize pressure changes
- Measurements of the shallow strain tensor could replace some deep monitoring wells during characterization and monitoring

USING THE SHALLOW STRAIN TENSOR TO CHARACTERIZE DEEP GEOLOGIC RESERVOIRS

ABSTRACT

Storing and recovering water, carbon and heat from geologic reservoirs is central to managing resources in a changing climate. We tested the hypothesis that the strain tensor caused by injecting or producing fluids can be measured at shallow depths and interpreted to advance understanding of underlying aquifers or reservoirs. Geodetic-grade strainmeters were deployed at 30m depth overlying the Bartlesville Formation, a 500-m-deep sandstone near Tulsa, OK. The strainmeters are 220m east of injection well 9A completed in a permeable lens at the base of the Bartlesville Formation. Water was injected into well 9A at approximately 1.0 L/s during four tests that ranged in duration from a few hours to a few weeks. The horizontal strain increased (tension) and the circumferential strain was a few times larger than the radial strain. The vertical strain decreased (compression) during injection. Strain rates were approximately 100 nε/day during the first few hours, but the rates decreased and were approximately 10 nε/day during most of the tests. Four independent methods of poroelastic simulation and inversion predict reservoir properties and geometries that are similar to each other and consistent with independent information about the reservoir. All strain interpretations predict that a boundary to the permeable lens occurs beneath the vicinity of the AVN strainmeters, which is consistent with core data from the site. The boundary of the permeable lens is located by matching the radial and circumferential strains, which demonstrates the value of measuring the strain tensor.

PLAIN LANGUAGE SUMMARY

Storing and recovering water, carbon and heat from subsurface aquifers and reservoirs is central to managing resources in a changing climate. Pressure changes in a reservoir cause tiny

deformations in the reservoir itself, but the effects are also felt in overlying formations near the ground surface. The deformation is characterized at a particular location by strain of different magnitudes in different directions, which is referred to as the strain tensor. We used instruments called strainmeters to measure the strain tensor at shallow depths (30m) overlying a much deeper (500m) sandstone reservoir when water was injected into a well in Oklahoma. Injection into the reservoir caused stretching in the horizontal direction and vertical compression at the 30-m-deep strainmeter. We analyzed and interpreted the strain signal using four different mathematical methods. Interpretations of the shallow strain measurements are consistent with interpretations from more standard methods of reservoir characterization using deep monitoring wells. Shallow strain tensor measurements are cheaper and less risky than using deep monitoring wells. Our result is exciting because it suggests that strain tensor measurements could reduce risks of storing wastes, like CO_2, and improve the efficiency of managing critical subsurface resources in the future.

1 INTRODUCTION

Permeable formations in the subsurface can act as sources or short-term storage reservoirs for materials and energy that are strategically important resources (e.g., water, hydrocarbons, minerals, natural gas and heat). Likewise, these formations are also targeted for the permanent storage of CO_2, and various industrial and hazardous wastes. Effectively using permeable formations for resource recovery or storage requires characterizing the distribution of material properties, and monitoring subsequent fluid pressures. Material properties are estimated by calibrating reservoir models using data from transient well tests, which involve injecting into or pumping from one well while measuring the resulting pressure change in the active well and nearby observation wells in the formation. Observation wells in deep geologic reservoirs are nearly always sparsely distributed and are often not available at all, thus limiting the ability to monitor reservoir fluid pressures and resolve geologic complexities needed to predict flow and assess risks.

To address this shortcoming, some investigators have turned to measuring the deformation of geologic materials caused by pressure changes from well operations. Pressure changes deform the reservoir and overburden in a distinctive pattern that extends long distances from the reservoir itself. The assumption is that deformation measurements made at the ground surface or shallow depths can be used instead of data from deep monitoring wells to estimate formation properties and changes in fluid pressures. One of the most common instruments used to measure deformation is the borehole tiltmeter (Vasco et al. 1998, Fabian, 2004; Murdoch and Hisz, 2010). Other investigators have used InSAR or GPS to measure vertical displacements at the ground surface (Vasco et al. 2019; Burbey et al. 2006; Teatini et al. 2005). Another approach has used extensometers to measure uniaxial strain or displacement (i.e., expansion or contraction of the borehole) along the axis of a borehole (Pope and Burbey, 2004; Cappa et al., 2006; Svenson et al. 2008; Guglielmi, et al. 2013). Recent advances of this approach involve distributed measurements of uniaxial strain along a borehole using optical fibers (Xue and Hashimoto, 2017; Becker et al. 2017, Sun et al. 2020; Zhang et al. 2021). These investigations have measured one or two components of strain, displacement or tilt, but fluid injection or pumping creates a full strain tensor in a broad region around the well (Murdoch et al, 2020; fig. 3). This means that only a portion of the information embodied in the strain field has been

utilized by previous studies.

The geodetic community has developed accurate tools for measuring the strain tensor associated with earth processes (Sacks et al., 1971; Gladwin, 1984; Gladwin and Hart, 1985). Geodetic borehole strainmeters have been too expensive to warrant applications associated with aquifer or reservoir characterization, although their ability to generate useful data from pumping is known (Barbour and Wyatt, 2014). Recent advances in optical fiber sensors (DeWolf, 2014; Murdoch et al. 2019) have made it feasible to measure strain in boreholes with the precision of a geodetic-grade strainmeter, but at a small fraction of their complexity. The development of the optical fiber strainmeter has opened the possibility that it could be practical to measure at shallow depths the full strain tensor caused by injecting or pumping in deep reservoirs, but to our knowledge this approach has never been demonstrated.

The objectives of this study are to 1) demonstrate the feasibility of measuring the transient strain tensor at shallow depths in response to pressure changes in a subsurface reservoir, and 2) show how shallow strain tensor data can be interpreted to provide useful information about the properties of the underlying reservoir. The study was motivated by the need to reduce risks (e.g. leakage, induced seismicity) associated with CO_2 storage in geologic formations, but it is applicable to a wide range of processes involving reservoirs and aquifers.

2 METHODS

This investigation involved deploying strainmeters at shallow depths (~30m) at a well field in Oklahoma, injecting water at a selected well (well 9A in Figure 1c and d) while monitoring strain and pressure in the vicinity, and then interpreting the data using four independent methods.

2.1 Field Site

The project was conducted at the North Avant Field, an oilfield in Tiers 23N and 24N, Ranges 11E and 12E in Osage County, OK (Figure 1a), which was discovered more than 100 years ago and is currently operated by Grand Resources, Inc. Wells in the North Avant Field produce oil from the Bartlesville Formation, a sandstone of Pennsylvanian age on the northeastern side of the Oklahoma platform of the Cherokee Basin (Figure 1b). Our information about the Bartlesville Formation in the vicinity of the North Avant Field (Murdoch et al., 2019)

is from Obianyor (2008) and references cited therein, and from unpublished analyses by Grand Resources. That work indicates the Bartlesville Formation is essentially flat-lying (dip to the west-southwest at 1/100) and is approximately 30 m thick at the North Avant Field. The Bartlesville Formation includes three important stratigraphic units, an upper unit with bedforms typical of meandering fluvial facies, and a lower unit with cross-bedded sands typical of braided fluvial facies. These units are underlain and overlain by shale and claystone with low permeability.

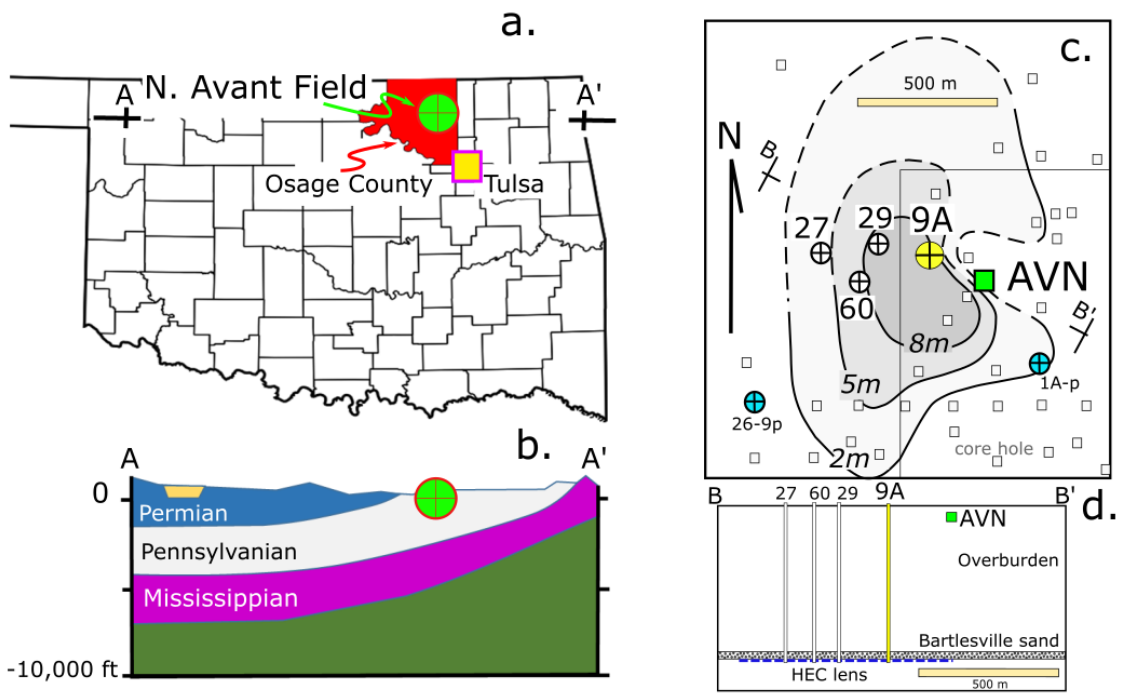

Figure 1. Location and geologic setting of the North Avant Field in Osage County, OK. (a) Regional map. (b) Regional cross section through A-A′. (c) Map of vicinity of strainmeters at location AVN (green) in the overburden above the Bartlesville Formation. Well 9A (yellow) was used for injection tests. Wells 27, 29, 60 (blue) were used for pressure monitoring. Wells 1Ap and 26-9p are water production wells. Contours are thickness in meters of coarse-grained HEC lens at base of the Bartlesville Formation, dashed where inferred. Thinnest line is the NW corner of Section 25, Tiers T24N, andR11E, which is shown to provide location.

The braided fluvial facies is underlain locally by a third stratigraphic unit consisting of elongate, coarse-grained lenses several hundred m wide and 1,000 m or more long that typically

trend approximately NE/SW (Figure 1c). These lenses are referred to as ``high energy channels'' (HEC) because the coarse-grained sediment they contain is inferred to have been deposited in an environment where the water flow was rapid, and thus at high energy. The HECs are inferred to include multiple channel deposits within paleo-valleys.

The HECs are the most productive oil-bearing units in the Bartlesville Formation. Their permeability is commonly more than 100 mD, and it is 1,000 to 2,000 mD in some locations. The porosity of these zones is typically greater than 20%. The permeability of the HECs can be two orders of magnitude greater than the overlying sandstone. The HECs are scattered, and their location and extent are difficult to predict. Identifying the location and geometry of the HECs is important to oil production operations because more mobile oil occurs within these permeable lenses compared to the overlying, finer-grained sandstones. Characterizing stratigraphic lenses similar to HECs during CO_2 storage is important because their properties and geometry would affect CO_2 transport.

Figure 2. Strainmeters used for the investigation. (a) Gladwin strainmeter being installed at the North Avant field, Oklahoma. (b) Cutaway view of the Optical Fiber Areal Strainmeter showing the sensing optical fiber coupled to the outer shell and the reference optical fiber separated mechanically by an air gap.

Well 9A was used during the project to inject water that was produced from pumping wells to the south and east (Figure 1c). Well 9A is a vertical well completed in a HEC at 530 m (1,700 feet) depth. Wells 1Ap and 26-9p (Figure 1c) are production wells that were in operation

during the field tests, and additional production wells were in operation to the south and east of well 9A (Murdoch et al. 2019). Water with a minor fraction of oil was pumped from those wells at rates that were essentially constant, and some of that water was reinjected into well 9A during the tests conducted for the project.

Analysis of cores and logs by Grand Resources indicates that well 9A intersects a HEC (Figure 1c) that is inferred to be 500 to 800 m wide, and up to 10 m thick. The HEC is bounded on the east and south by observations in cores, but the lateral boundary of the HEC to the north and west is poorly constrained. One of the goals of the project was to evaluate the feasibility of characterizing the HEC using strain data and to evaluate more accurately of the HEC to the north and west, where the direct data is only sparsely available.

2.2 Site layout

Strain was measured at a depth of 30 m at the three strainmeters and tiltmeter at location AVN approximately 220 m east of well 9A (Figure 1c). Pressure was measured in wells 27, 29 and 30 using logging transducers, which were suspended below the static water level (approximately 150 m below ground). The pressure monitoring wells are at the following radial distances from well 9A: well 29, r = 190m; well 60, r = 270 m; well 27, r = 370m. All three of the pressure monitoring wells and well 9A are inferred to be completed within the same permeable HEC lens (Figure 1d).

2.3 Strain Instruments

Four instruments to measure strain and tilt were deployed at location AVN and used during the injection tests (Murdoch et al., 2019).

1. Gladwin Tensor Strain Meter (Figure 2a) obtained from UNAVCO.
2. Optical Fiber Areal Strainmeter developed for the project.
3. Grout-in Eddy Current Tensor Strain and Tilt System developed for the project.
4. LILY tiltmeter obtained from vendor (Applied Geomechanics/Jewell Instruments).

All the instruments consist of sensors used to measure strain or tilt, and a package of electronics used to measure the signal from the sensor. The sensing packages are inside steel tubes (Figure 2), which are placed in borings and coupled to the enveloping rock. Most of the instruments are coupled to rock using expanding grout that permanently anchors the instrument

in the boring, but the LILY tiltmeter was coupled using sand so it could be removed.

2.3.1 Gladwin Tensor Strain Meter (GTSM)

The sensing package of the GTSM is a stainless steel tube (Figure 2a) with four custom capacitance gauges oriented at different angular positions (Gladwin and Hart, 1985). The gauges are connected to electronics at the ground surface where small changes in capacitance are measured. Displacements measured by the four gauges are used to resolve the strain tensor normal to the axis of the tube.

The resolution of the GTSM is 10^{-11} strain, or 10 picostrain (least-count) with a linear dynamic range of up to 10^{-3} strain when operating with its lowest gain transformer. More than 70 GTSMs have been installed in the U.S. by UNAVCO (unavco.org) and dozens of others have been installed in other countries and used to measure strain caused by tectonics. This experience has made the GTSM the *de facto* standard in high resolution in-situ strain measurement.

2.3.2 Optical Fiber Areal Strainmeter (OFAS)

The Optical Fiber Areal Strainmeter (OFAS) is similar to the GTSM in that it consists of a down-hole sensing package connected to an up-hole electronic interrogator. However, unlike the electronic sensors used by the GTSM, the sensing package of the OFAS contains only optical components. The strain measurement is made by wrapping two cylindrical mandrels with equal lengths of optical fiber (Figure 2b). The outer mandrel contains the sensing fiber and is coupled to the formation with expanding grout. An inner mandrel contains a reference optical fiber that is decoupled from the outer mandrel by an air gap. The optical fibers on the two mandrels are joined by a 3x3 optical coupler that is connected to optical fibers that extend up to the interrogator. Laser light from the interrogator is split at the coupler and the fibers on the two mandrels create an equal-arm Michelson interferometer. Changes in the length of the sensing fiber are measured by comparing to the length of the reference fiber using laser interferometry. Versions of this operating principle have been used in optical fiber hydrophones (Bucaro et al., 1977; Rashleigh, 1985), aero-acoustic sensors (Bucaro et al., 1979; Zumberge et al., 2003), and in a borehole strainmeter (DeWolf, 2014).

The optical interrogator is the active electronics package used to measure strain in the passive down-hole sensing package (only the down-hole package is shown in Figure 2b). Its

purpose is to transmit coherent, monochromatic laser light to the down-hole optics and demodulate the returning interference fringes into an optical phase signal linearly proportional to the strain in the formation. The interrogator was developed for this work and designed to fit in a 10-cm-diameter tube suspended a few meters below the ground surface inside the casing. This is deep enough to significantly dampen the temperature changes at the ground surface, but shallow enough so the interrogator can be easily retrieved.

The least-count resolution of the OFAS is approximately $6x10^{-15}$ strain, or 6 femtostrain, nearly 2,000 times more sensitive than the GTSM. The dynamic range is determined by the maximum strain rate, which is roughly 10^{-4} 1/s, resulting in an effective bit depth of ~34 bits at 1 Hz.

2.3.3 Grout-in Eddy Current Strain and Tilt Instrument (Eddy Current Instrument)

The eddy current instrument uses eddy current sensors, which are electronic sensors similar to the capacitance gauges used by the GTSM. The eddy current sensors used in this instrument were obtained from a commercial vendor, which reduces costs and simplifies construction compared to the custom capacitance gauges used in the GTSM. One drawback to the commercial eddy current gauges is that they must be connected to signal conditioning electronics over a cable with a maximum length of several meters. The instrument was designed with the electronics in a second steel cylinder located above the sensing package. One advantage of the commercial gauges is that they are compact and easy to deploy, and this allowed us to configure the eddy current instrument to measure the horizontal and vertical components of the strain tensor and two components of tilt.

The nominal strain resolution of the eddy current instrument is approximately 10^{-8}, or 10 nanostrains, in the horizontal and about 1 nanostrain in the vertical, with a dynamic range of up to 2.5×10^{-3} strain. The tilt resolution is approximately 0.3 – 0.6 nanoradians with a dynamic range of up to 3 to 6×10^{-3} radians.

More information on the design and performance of the OFAS and eddy current instruments is described by DeWolf in Chapter Two of Murdoch et al. (2019).

2.3.4 LILY Electrolytic Tiltmeter

The LILY tiltmeter uses an electrolytic sensor that has been the mainstay of precision borehole tiltmeters for several decades (Evans et al., 1982; Castillo et al., 1997). This instrument contains two orthogonal sensors with a resolution of up to 5 nanoradians and a dynamic range of up to 330 microradians (~16-bit resolution). We deployed a LILY tiltmeter to provide baseline data for evaluating the tilt signal from the eddy current instrument.

2.4 Deployment

The three strainmeters were deployed in 0.15-m-diameter borings separated by approximately 10m. An initial boring drilled to approximately 70-m depth encountered soft shale and a more resistant limestone bed between 27 and 30m depth. The borings were cased with steel pipe to a depth of approximately 20 m. The instruments were lowered to the middle of the limestone layer and the open intervals were filled with BASF 1206 Masterflow grout, which expands slightly as it cures (https://www.master-builders-solutions.com/en-us/products/grouts/cementitious-grouts/masterflow-1206). Electronics packages were connected to a telemetry system powered by solar cells, and the data are available at http://ds.iris.edu/mda/2J/. Strain data from the Gladwin strainmeter are available at https://www.unavco.org/data/strain-seismic/bsm-data/bsm-plot-listing.html?sid=AVN2.

2.5 Signal Processing

Signal processing is required to generate a dataset suitable for analysis. The processing includes 1.) calibrating the output of the instrument to strain. 2.) identifying and removing strains caused by changes in barometric pressure; 3.) identifying and removing strains caused by the solid Earth tides; 4.) discarding long-period background signals (detrending); 5.) reconciling gaps in the data. The instruments were initially calibrated in the lab, but then they were recalibrated after deployment by comparing their output signals to calculated Earth tides, and to teleseisms. Signal processing methods are based on procedures established by Hodgkinson (2006), and Langbein (2010).

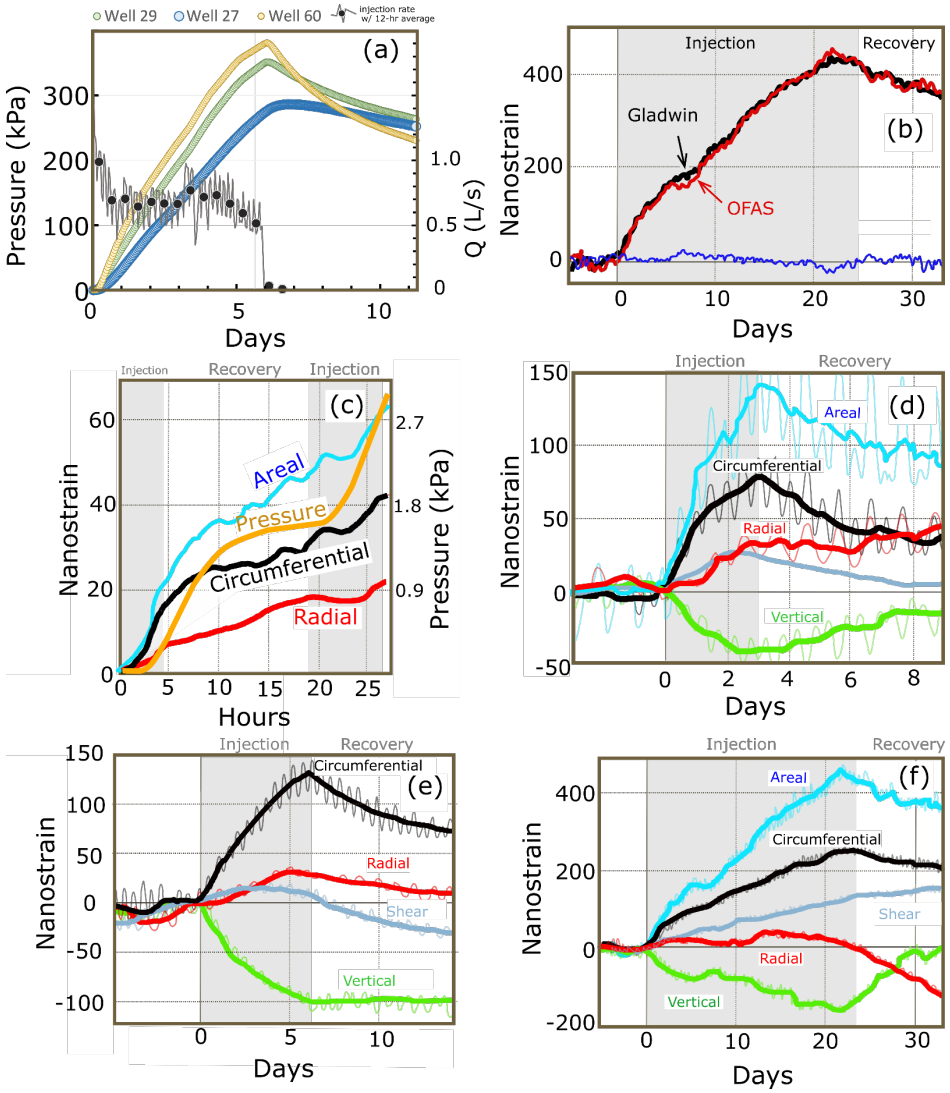

Figure 3. Time series of pressures, injection rates and strains. (a) Injection rate and pressure during Oct 2017 injection test at North Avant Field, OK. (b) Areal strains during July 2018 injection. Injection occurred during gray band. Day 0 is June 28th, 2018. Semitransparent lines are raw data, solid lines have earth tides, barometric effects and long-term trends removed. Areal strain measured with the OFAS (red line), and with the Gladwin GTSM (black line). The residual (GTSM-OFAS) as blue line. (c) Strains measured at AVN2 and pressure measured at well 29 during and following injection for 4 hours (grey) and 7 hrs (grey) at well 9A in July 2017. Strain tensor during and following injection for (d) 3 days in Nov. 2017; (e) injection for 6 days in Oct 2017; (f) injection for 25 days in June-July 2018.

3 RESULTS

Details of the pressure and rate varied slightly during the well tests (Figure 3), but a test conducted in October 2017 is representative (Figure 3e). The horizontal strains were tensile and the magnitude of the circumferential strain was greater than the radial strain. The ratio

radial/circumferential strain is 0.2 to 0.5. The vertical strain was compressive and was greater than the radial, but less than the circumferential strain. A principal strain direction was assumed to be vertical because of the shallow depth of the measurement, and this implies that the instruments measure the full strain tensor. The small values of horizontal shear strain (Figure 3) indicate that the principle horizontal strains are approximately aligned with the cardinal directions. The strain rate was as fast as 100 nε/d during the first several hours of injection, but it slowed with time and was approximately 30 nε /d during the first day, and 10 nε/d after the first week (Figure 3).

Data from the Gladwin strainmeter were processed to determine the areal strain and these results were compared to data from the OFAS. The results from the two instruments are virtually identical (Figure 3b).

3.1 Strain Type Curves

The simplest method of analyzing strain data was derived by adapting the type-curve approach to analyzing pressure transients during well tests (Murdoch et al, 2021). This approach was motivated by the observation that the normal strains during the well tests were approximately a linear function of the log of time (Figure 4a and b), which is similar to pressure type-curves (Cooper and Jacob, 1946).

The data indicate that the magnitude of the semi-log slopes of the normal strains increase and are roughly constant for $t/r^2>2$, where r is the radial distance of the measurement location, and the pressure signals follow a similar pattern (Figure 4a). Interestingly, the zero-strain intercept for the vertical strain is equal to the intercept for the average horizontal strain, although the signs and slopes of the two strains are different and they were measured by instruments in two different boreholes.

Hydraulic diffusivity can be estimated from average horizontal normal strain data when the measurement location is sufficiently far from the injection well (Murdoch et al. 2021). This indicates the hydraulic diffusivity is in the range, $0.5 < D_h < 0.6$ m^2/s. For comparison, analysis of pressure data indicates, $0.2 < D_h < 0.7$ m^2/s (Murdoch et al. 2021).

The semi-log slopes of the pressures at the monitoring wells approximately double for $2 < t/r^2 < 6$, and the slope of the average horizontal strain (half of the areal strain) abruptly

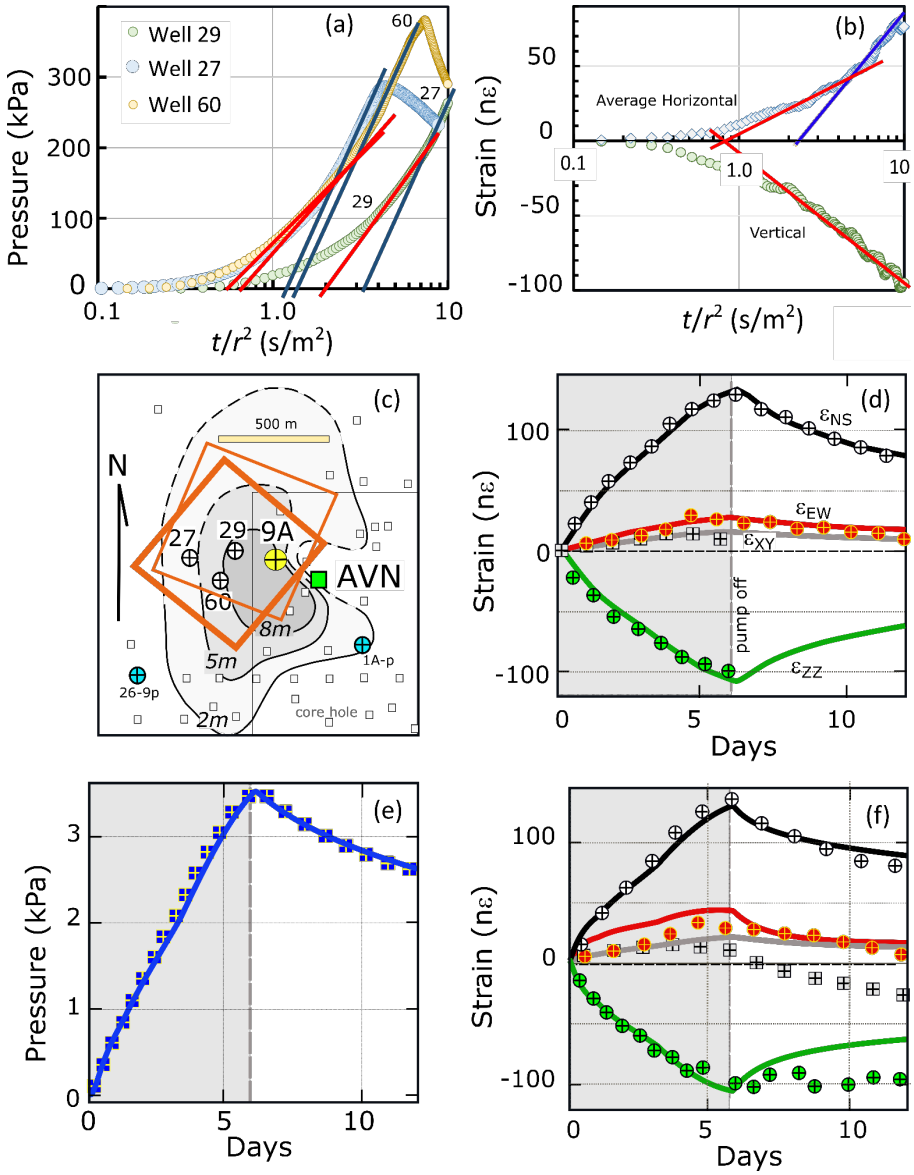

Figure 4. Results from analyses of strain and pressure. (a) Drawdown in wells 27, 29, and 60. Red line is the best fit to first, blue line is best fit to second straight section (Murdoch et al., 2021). (b) Average horizontal and vertical strain with straight sections as in (a) based on Murdoch et al. (2021). (c) Boundaries of the permeable HEC lens from the October 2017 (thick orange line) and November 2017 (thin orange line) tests based on the analytical model. (d) Strain time series during the October 2017 test (points) and results from the analytical model (solid lines). (e) Pressure data from well 29 (points) and simulated with 3D poroelastic model using manual calibration (lines). (f) strain tensor data from AVN (points) and simulated using 3D poroelastic model (lines). Vertical and shear strains after the pump was turned off were ignored.

increases at $t/r^2 \sim 4$ (Figure 4a). One interpretation of this increase in the semi-log slope of the pressure during a well test is that the drawdown is affected by a lateral boundary (Streltsova, 1982). The hydraulic diffusivity and time of the change in slope of the pressure data can be used to infer the distance to the boundary as $L_b \approx 220$ to 400 m (Murdoch et al. 2021). Using the change in slope of the semi-log strain data indicate that $L_b \approx 290$ to 320m.

These results indicate that the hydraulic diffusivity and distance to the boundary of the reservoir estimated using standard well testing methods are essentially the same as the values estimated using a type-curve-like method of analyzing the shallow normal strain data.

3.2 Analytical model

Analytical solutions are a mainstay of techniques for evaluating pressure signals measured during well tests, and similar methods can be used to evaluate the poroelastic response. The approach we used is to consider the portion of the aquifer or reservoir affected by a well as a pressurized poroelastic region, V, in a homogeneous, isotropic elastic half-space (Figure 5). The half space geometry allows the effects of the ground surface to be included. The simplest case is to represent the region as a pressurized cuboidal *inclusion* where the elastic properties are the same as those of the enveloping half-space (host) material. The properties of the reservoir may actually be quite different from those of the confining unit, so the next step is to represent the region as a pressurized cuboidal *inhomogeneity* where the elastic properties differ from the enveloping host material. The inclusion model will be outlined first, followed by the inhomogeneity model. In both cases, the pressure change, Δp, in the region is assumed to be uniform and equal to the pressure data from the monitoring wells (Figure 1c).

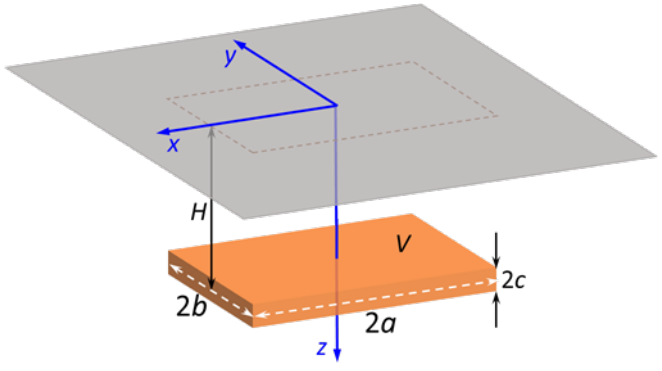

Figure 5. A model of a pressurized reservoir represented by a poroelastic cuboidal inclusion (the same properties of reservoir and host rock) or inhomogeneity (different properties of reservoir and host rock) in an elastic half space.

3.2.1 Inclusion model

When the pressurized region has the same properties as those of the host material, the deformation induced in the half-space (Figure 5) by the pressure change can be found by using Mindlin and Cheng's (1950) results. They studied the elastic effect of a non-uniform distribution of temperature in a half-space, but thanks to the mathematical similarity between the thermoelastic and poroelastic constitutive laws (Cheng, 2016), one only needs to replace parameter β in the Mindlin and Cheng (1950) equation (2) with $\beta = \alpha\Delta p/(\lambda + 2\mu)$, where Δp is the pressure change distribution, α is the Biot-Willis coefficient, $\mu = E/[2(1+\nu)]$ and $\lambda = 2\mu\nu/(1-2\nu)$ are the Lame parameters, E is the Young Modulus, and ν is the Poisson ratio. Equation (2) in Mindlin and Cheng (1950) expresses the induced displacement vector at the arbitrary point in the half-space through a full-space Newtonian potential. For a uniform pressure change, Δp, in the inclusion, zero pressure change in the envelopoing material, and cuboidal inclusion shape (Figure 5), this potential is expressed in closed form (MacMillan's, 1958, §43, page 58). Once the displacement field is known, the induced tilts and strains are found in closed form by differentiating displacements (Landau and Lifshitz, 1986).

3.2.2 Inhomogeneity model

If the pressurized region and the host material have different properties, the former is called an inhomogeneity (Eshelby, 1957). The vertical deformation of a *thin* pressurized inhomogeneity (Figure 5) follows from the solution outlined in Germanovich and Chanpura (2002) as

$$\varepsilon_{zz} = \frac{\Delta c}{c} = \frac{\alpha_0 \Delta p}{\lambda_0 + 2\mu_0} \tag{1}$$

All other strains in the inhomogeneity are negligible in the leading order. Hereafter, subscript "0" denotes material properties of the inhomogeneity whereas the lack of subscript indicates properties of the enveloping material.

According to (1), the vertical deformation caused by a thin pressurized inclusion is

$$\varepsilon_{zz} = \frac{\Delta c}{c} = \frac{\alpha \Delta p_*}{\lambda + 2\mu} \tag{2}$$

whereas other strains in the inclusion are negligible in the leading order. The final step is to recognize that the analysis for the homogeneous case can be applied to the heterogeneous case by equating (1) and (2). This gives the pressure change

$$\Delta p_* = \frac{\alpha_0(\lambda + 2\mu)}{\alpha(\lambda_0 + 2\mu_0)}\Delta p \qquad (3)$$

that should be used in the homogeneous case to account for contrasts in elastic properties between the inhomogeneity and matrix. Deformations determined in this way will be accurate in the leading terms both in the confining formation and in the pressurized reservoir.

A forward model that predicts strains was developed from the analytical solution by assuming the pressure in the reservoir is uniform over a cuboidal region, and the pressure is given by the data from monitoring well 60 (Figure 1). A cuboid geometry was selected because it resembles an HEC lens. The Levenberg–Marquardt (Aster et al., 2013) inversion algorithm was used to estimate reservoir location, orientation, and dimensions, and elastic properties of the reservoir and overburden.

The inverse analysis was able to find parameters that cause the analytical solution to fit the observed strain data remarkably well (Figure 3d). A variety of initial estimates were used to avoid local minima. The inversion estimated that the horizontal dimensions of the lens are between 500 m and 600 m, the thickness is approximately 9 m, and Young's modulus is $E = 3$ GPa. Data from another injection test in November 2017 were analyzed using the same approach and the size and location of the lens are similar (Figure 3d).

3.3 3D Numerical Model

A 3D numerical model was used to solve the governing equations from poroelasticity using boundary conditions that represent the Bartlesville Formation as a uniform layer beneath a uniform overburden. The model was set up using Comsol Multiphysics using the same approach described in Murdoch et al., (2019; Chapter 5; 2020; and 2021). The HEC lens was represented using the same cuboidal shape as the HEC lens in the analytical model, but the 3D numerical model calculates the pressures instead of extrapolating them from the data. Parameters were adjusted manually to fit the observed strains and pressures.

The results indicate that both pressure and strain data can be predicted with normalized fit standard errors of a few percent (Figure 4e and f). The analysis indicates that the Young's modulus, *E*, of the HEC lens is 2 GPa, thickness is 5m, and the maximum length of the HEC lens is 570 m, which are similar to results from the analytical solution.

3.4 Stochastic Inversion

The most detailed interpretation of the strain and pressure data uses stochastic inversion with a 3D numerical poroelastic simulator called Geocentric (White and Borja, 2008, 2011) configured to represent conditions at the North Avant Field. The geometry of the HEC lens was constrained using a sequence of three progressively more general assumptions. The analysis first found parameters that fit the data using a circular-cylinder lens geometry. The geometry was then assumed to be an elliptical cylinder with an arbitrary location and orientation and the results from the circular lens were used as initial estimates. Finally, this process was repeated by adding or removing material along the outer edge of best fitting datasets for the elliptical lens. This resulted in lenses with irregular shapes.

The goodness-of-fit between the observed and predicted strains and pressures was determined initially using parameters selected by Latin Hypercube sampling (Iman et al., 1980). Regions of the parameter space where the fit was relatively good were then searched using the Non-dominated Sorting Genetic Algorithm II (NSGAII), (Deb2002a), a multi-objective genetic algorithm, to refine the best-fitting parameters sets. The total analysis required 67,310 simulations with approximately 20,000 simulations during the evaluation of each of the circular, elliptical, and irregular lens geometries (Murdoch et al. 2019).

The goodness of fit was improved as the analysis progressed from representing the HEC lens with a circular to elliptical to irregular geometry. A final result that used both pressure and strain data produced 1886 samples of the model parameters (Figure 6a) and HEC lens geometries. An example of one of estimated HEC lens geometries is approximately 500 m in maximum dimension with a permeable band that trends approximately N60E (Figure 6b). The

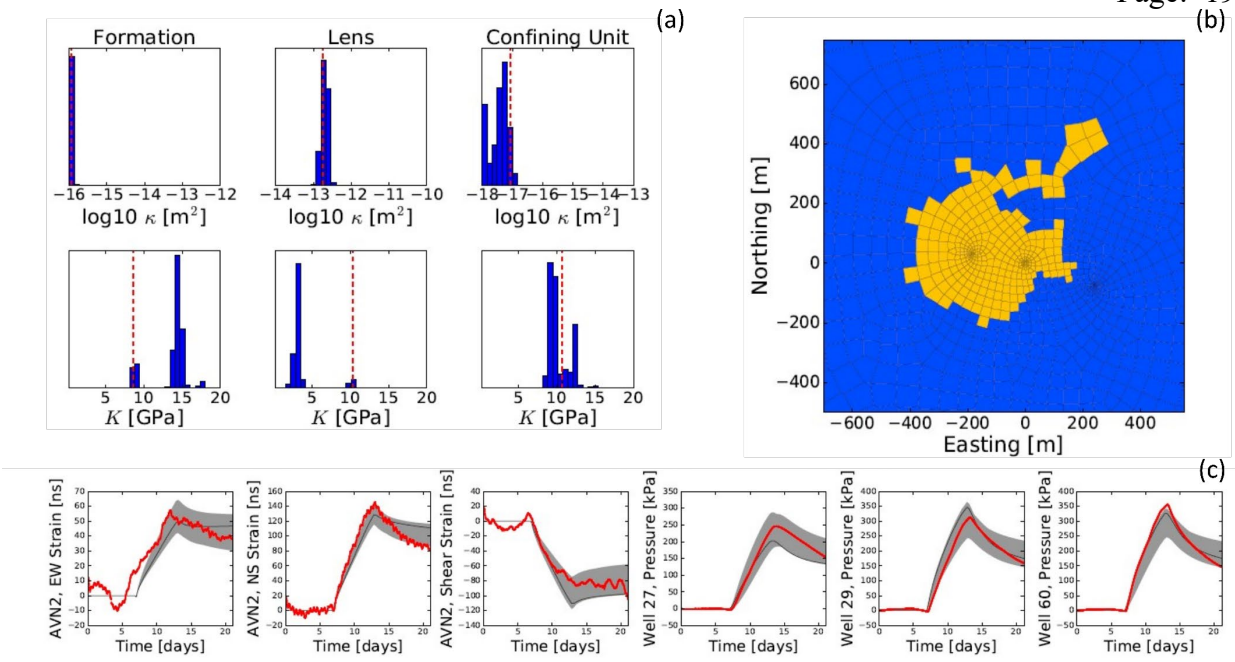

Figure 6. Results for the irregular geometry used to interpret the Oct 2017 injection test at well 9A. (a) Parameter distributions for the best fitting parameter sets selected by the stochastic optimization algorithm; dashed red lines indicate specific values for the sample associated with the HEC lens geometry shown in (b). (c) Observed strain and pressure data are shown in red with the simulation results for the example lens geometry and indicated parameter values shown in black. The simulation results for the full ensemble of 1886 parameter samples are shown as grey band that envelopes the observed results.

simulated strain and pressure responses generally follow the trends in the data, and the full ensemble of 1886 accepted samples forms envelopes that fully contain the observed pressure and strain data (Figure 6c). More results given in Murdoch et al. (2019, Chapter Five) show different parameter sets and geometries, but the results are similar to Figure 6.

4 Discussion

The shallow strain tensor measured during injection tests was analyzed using different methods and the results are generally consistent with each other (Table 1), and with independent information characterizing the subsurface in the field area (i.e., well logs, core). Results indicate the hydraulic diffusivity of the reservoir is approximately 0.5 m^2/s and the permeability is between 100 and 500 mD, which is consistent with measurements of permeability from cores taken in the vicinity of well 9A (Obianyor, 2008), and with analyses of pressure transients during well tests.

The four methods of analysis indicate that the Young's modulus of the HEC lens is

Table 1. Parameters estimated using different forward models, lens geometries and inversion methods. [a]: parameter value assumed. -: parameter not estimated.

	Forward model		Type	Analytical	Numerical	Numerical	Numerical
	Lens geometry		Circular	Rect.	Rect.	Elliptical	Irregular
	Inversion method		Graphical	Gradient	Manual	Stochastic	Stochastic
Parameter	*Location*	*Units*					
Young's Modulus	HEC Lens	GPa	-	2	2	2-3,4-6	6
	Bartlesville	GPa	-	-	8	17-22	33
	Confining	GPa	-	-	2.9	17-22	33
Permeability	HEC Lens	mD	100	-	500	250	150
	Bartlesville	mD	-	-	5	0.1	0.1
	Confining	mD	-	-	0.01	0.003	0.003
Thickness	HEC Lens	mD	-	7	5	5[a]	5[a]
Hyd. Diffusivity	HEC Lens	m^2/s	0.5	-	0.6	0.9	0.8
	Bartlesville	m^2/s	-	-	0.04	-	-
Dist. to boundary	East of 9A	m	500	120	80	100	120
Dist. to boundary	North of 9A	m	500	225	150	200	400
Dist. to boundary	South of 9A	m	500	345	150	150	150
Dist. to boundary	West of 9A	m	500	390	500	400	400

between 2 and 6 GPa. This is somewhat softer than moduli estimated from laboratory tests we conducted on cores from the Bartlesville Formation, which give $E \sim 10$ GPa, but this is likely because the laboratory tests were biased by preferential selection and testing of the most well indurated intervals in the cores.

Strain interpretations indicate the maximum dimension of the permeable lens is 500 to 1,000 m (Figure 7). An isopach map of coarse-grained sand indicates a feature that is roughly 1,000 m in extent, although data constraining the extent are sparse to the north and west (Figure 7).

All the interpretations indicate that a boundary of the permeable lens occurs in the vicinity of the region underlying strainmeters at AVN (Figure 7). The boundary is east of well 9A and four different inversion methods predict the boundary is between 80 and 120 m from well 9A (Table 1). The Type Curve method gives a larger value (Table 1), but it assumes the lens is 1D and centered on well 9 whereas the other methods allow the locations of each boundary to vary. The location of the boundary estimated by inversion is remarkably consistent between the methods because a boundary in this location is required for the poroelastic analysis

to correctly predict the relative magnitudes of the observed radial and circumferential horizontal strains (Figure 3). A boundary in the reservoir reduces the magnitude of the radial strain relative to the circumferential strain at shallow depth in the simulations, which explains the field data. Locating a reservoir boundary is an example of the value of measuring the full strain tensor.

The horizontal strain tensor data shown here were measured with a geodetic-grade Gladwin strainmeter, which is out of reach of most well testing applications and is currently unavailable commercially. However, the areal strain data measured with OFAS are virtually identical, but with lower noise than the strain measured by the Gladwin strainmeter (Figure 3b). We have shown that the OFAS technology with design modifications can be used to measure the horizontal strain tensor. The OFAS technology is virtually immune to electrical interference that can damage electronics, and it is simpler to construct than instruments using electronic sensors, like the Gladwin strainmeter.

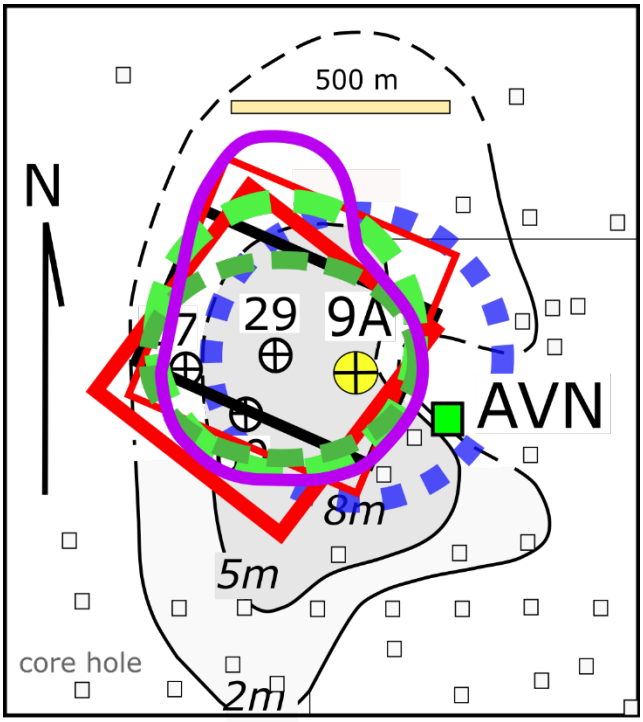

Figure 7. The extents of a permeable HEC lens in the vicinity of well 9A based on interpretations of injection tests at well 9A. The inferred extents are consistent between the methods of interpretation. Extent inferred from strain type curve: purple dotted line; analytical solution for poroelastic inclusion: thick red line from Oct. 2017 test, thin red line from Nov. 2017 test; manual fit of 3D numerical model: black line; stochastic inversion using circle: green dashed line; ellipse: dark green dashed line); or irregular geometry: purple line. Contours and grey scale are the isopach of the permeable lens identified in core or well logs, dashed where inferred.

The OFAS measures strain with an equal-arm Michelson interferometer created with optical fibers, which differs fundamentally from the physics used by other techniques for measuring strain with optical fibers (Fiber Bragg Gratings, Brillouin, phase OTDR, OFDR, etc.). One important consequence is that the precision of the equal-arm Michelson interferometer can be significantly greater than that of other optical fiber strain sensing methods. This makes it well suited to

characterizing small strains caused by subtle subsurface processes. Another difference is in the electronic interrogator needed to measure strain. The optical and electronic components used in the OFAS interrogator are more compact, simpler, and draw less power than those used in other strain sensors. This makes it feasible to package the electronics in a narrow tube that can fit into a well casing and be powered by a modest solar cell.

Measuring the strain tensor with optical fiber sensors also has limitations. The approach we used is intended to measure the strain tensor at several locations, instead of measuring uniaxial strain distributed at many locations, which is the approach used by other optical fiber strain sensors. This makes distributed strain sensing well suited to measure basic aspects of a transient strain field distributed in space, and applications of distributed strain sensing have capitalized on this aspect by measuring strain or acoustic signals distributed at hundreds or more locations along optical fiber in boreholes (Xue and Hashimoto, 2017; Becker et al. 2017), or in networks of trenches (Yavuz, et al. 2018). Another limitation to using low frequency to quasi-static strain tensor data is the need to remove strains caused by earth tides, barometric pressure fluctuations, rainfall, and other processes unrelated to changes in reservoir pressure. Signal processing methods for removing these signals are available (Murdoch et al., 2019), however, so this should not restrict application. We view the high resolution, transient strain tensor measured with the technology described here as a dataset that should complement the distributed strains measured with currently available methods (distributed optical fiber strain, tiltmeters, seismometer, InSAR, GPS or related).

5 CONCLUSIONS

Demands for clean energy, CO_2 storage, and a reliable water supply increase the need to efficiently characterize and monitor subsurface formations. We demonstrated that the strain tensor measured at shallow depth (30m) caused by pressure changes in a much deeper (530m) reservoir can be measured using high resolution strainmeters. The transient strain tensor data can be interpreted using several different techniques to estimate reservoir properties and reservoir geometries (e.g. boundaries) that are consistent with each other and with independent field information about the reservoir. This is significant because it provides a new technology with the potential to improve the recovery of resources and storage of wastes.

ACKNOWLEDGEMENTS

There are no financial conflicts of interests for any author. We appreciate logistical support and access to the North Avant Field provided by Marvin, Richard and Scott Robinowitz, Grand Resources Inc.

OPEN RESEARCH Data are available at http://ds.iris.edu/mda/2J/ .

REFERENCES

Aster, R.C. B. Borchers. C. H. Thurber. 2012. Parameter Estimation and Inverse Problems, 2nd edition. Academic Press, ISBN 9780123850485, 376 pp.

Barbour, A. J., and F. K. Wyatt (2014), Modeling strain and pore pressure associated with fluid extraction: The Pathfinder Ranch experiment, J. Geophys. Res. Solid Earth, 119, 5254–5273, doi:10.1002/2014JB011169.

Becker, M., Ciervo, C., Cole, M., Coleman, T., Mondanos, M. (2017) Fracture Hydromechanical Response Measured by Fiber Optic Distributed Acoustic Sensing at milliHertz Frequencies: Fracture Hydromechanics from DAS. Geophysical Research Letters, v44. 10.1002/2017GL073931.

Bucaro, J.A., H.D. Dardy, E.F. Carome. 1977. Optical fiber acoustic sensor. Appl. Opt. Jul. 1 16(7), 1761-2.DOI: 10.1364/AO.16.001761.

Burbey, T.J., S. M. Warner, G. Blewitt, J.W. Bell, E. Hill, 2006. Three-dimensional deformation and strain induced by municipal pumping, part 1: Analysis of field data. Journal of Hydrology, v. 319, Issues 1–4, 2006, p. 123-142, doi.org/10.1016/j.jhydrol.2005.06.028.

Cappa, F., Guglielmi, Y., Gaffet, S., Lancon, H., and Lamarque, I. (2006). Use of in situ fiber optic sensors to characterize highly heterogeneous elastic displacement fields in fractured rocks. International Journal of Rock Mechanics & Mining Sciences, Vol. 43, No. 4, pp. 647-654.

Castillo, D., Hunter, S., Harben, P., Wright, C., Conant, R., and Davis, E. (1997). Deep hydraulic fracture imaging: Recent advances in tiltmeter technologies. Int. J. Rock Mech. & Min. Sci., 34:3-4, Paper No. 047.

Cheng, A.H.D., 2016, Poroelasticity, Springer, 877 pp.

Cooper, H.H., and Jacob, C.E. (1946) A generalized graphical method for evaluating formation constants and summarizing well field history, Am. Geophys. Union Trans., vol. 27, pp. 526-534.

Deb K, Pratap A, Agarwal S, Meyarivan TAMT (2002) A fast and elitist multiobjective genetic algorithm: NSGA-II. IEEE Trans Evol Comput 6(2):182–197.

DeWolf, S. (2014). Optical Fiber Sensors for Infrasonic Wind Noise Reduction and Earth Strain Measurement. Doctor of Philosophy in Oceanography, University of California San Diego. http://roger.ucsd.edu/record=b8191107~S9.

Eshelby, J.D., 1957, The determination of the elastic field of an ellipsoidal inclusion and related problems. Proc. Roy. Sot. (London), Vol. A241, pp. 376–396.

Evans, K., Holzhausen, G., and Wood, M. (1982). The geometry of a large-scale nitrogen gas hydraulic

fracture formed in devonian shales: An example of fracture mapping using tiltmeters. Soc. Pet. Eng. J., 22, 755-763.

Fabian, M. (2004). Near surface tilt and pore pressure changes induced by pumping in multi-layered poroe- lastic half-spaces, number 229 in berichte ausdem fachbereich geowissenschaften. Universität Bremen. Doctoral thesis, Rheinische Friedrich-Wilhelms-Universität Bonn, ISSN: 0931-0800.

Germanovich L.N., and R.A. Chanpura, 2002, Modeling Thin Inclusions in Poroelastic Medium by Line Discontinuities, IUTAM Symposium on Analytical and Computational Fracture Mechanics of Non-Homogeneous Materials, B.L. Karihaloo (ed.), Kluwer, Dordrecht, Boston, London, pp. 133 – 142.

Germanovich, L.N., Gence, G., Lowell, R.P., Rona, P.A., 2012, Deformation and surface uplift associated with serpentinization at mid-ocean ridges and subduction zones, J. of Geoph. Research, Vol. 117, Issue B7, July 2012, DOI: 10.1029/2012JB009372.

Gladwin, M. T. (1984). High-precision multicomponent borehole deformation monitoring. Review of Scien- tific Instruments, 55(12):2011–2016.

Gladwin, M. T., and R. Hart (1985), Design parameters for borehole strain instrumentation, Pure and Applied Geophysics, 123, 59-80.

Guglielmi, Y. F. C., Lançon, H., Janowczyk, J. B., Rutqvist, J., Tsang, C. F., and Wang, J. S. Y. (2013). Isrm suggested method for step-rate injection method for fracture in-situ properties (simfip): Using a 3-components borehole deformation sensor. The ISRM Suggested Methods for Rock Characterization, Testing and Monitoring, pp 179-186. July 2014.

Hisz, D. B., Murdoch, L. C., and Germanovich, L. N. (2013). A portable borehole extensometer and tiltmeter for characterizing aquifers. Water Resources Research, 49, 1-11, doi:10.1002/wrcr.20500.

Hodgkinson, K. 2006. Procedures for processing borehole strainmeter data v1.1. UNAVCO report. https://www.unavco.org/projects/project-support/borehole-services/lib/docs/BSM_Processing.pdf.

Kumpel, H.-J., Varga, P., Lehmann, K., and Mentes, G. (1996). Ground tilt induced by pumping – prelimi- nary results from the nagycenk test site, hungary. Acta Geodaetica et Geophysica Hungarica, 31:67-78.

Landau, L.D., and E.M. Lifshitz, 1986, Theory of Elasticity, Volume 7 of A Course of Theoretical Physics, Third edition, Pergamon Press, Oxford, 187 pp.

Langbein, J. 2010, Effect of error in theoretical Earth tide on calibration of borehole strainmeters. Geophysical Research Letters, v. 37, L21303. doi.org/10.1029/2010GL044454.

MacMillan, 1958, The theory of the potential, Dover Publications, Inc., New York, New York, 384 pp.

Mindlin R.D., Cheng D.H. 1950, Thermo-Elastic Stress in the Semi-Infinite Solid, J. Applied Phys., 21(9), pp. 931-933.

Murdoch, L. C., Germanovich, L. N., Roudini, S., DeWolf, S. J., Hua, L., & Moak, R. W. (2021). A type-curve approach for evaluating aquifer properties by interpreting shallow strain measured during well tests. Water Resources Research, 57, e2021WR029613. http://10.1029/2021WR029613

Murdoch, L., Germanovich, L., Moysey, S., Hanna, A., Kim, S., Dewolf, S., Ebenhack, J., and Skawski, G. (2015a). Proof-of-feasibility of using wellbore deformation as a diagnostic tool to improve co2 sequestration. Final Report for Project DE FE0004542. U.S. Department of Energy. 276 pp.

Murdoch, L., Hisz, D., Ebenhack, J., Fowler, D., Tiedeman, C., Germanovich, L., et al. (2009). Analysis of hydromechanical well tests in fractured sedimentary rock at the nawc site, new jersey. In 43rd US

Rock Mechanics Symposium & 4th US-Canada Rock Mechanics Symposium. American Rock Mechanics Association.

Murdoch, L.C, Scott DeWolf, Leonid Germanovich, Alex Hanna, Robert Moak and Stephen Moysey. (2019). Characterizing and Interpreting the In Situ Strain Tensor During CO2 Injection. Final Report for DOE Project DE-FE 0023313, 252 pp.

Murdoch, L.C. L. N. Germanovich, S. J. DeWolf, S.M.J. Moysey, A.C. Hanna, S. Kim, R.G. Duncan, (2020). Feasibility of Using In Situ Deformation to Monitor CO2 Storage. International Journal of Greenhouse Gas Control, v. 93. 102853. https://doi.org/10.1016/j.ijggc.2019.102853.

Pope, J.P., and T.J. Burbey, (2004). Multiple-Aquifer characterization from single borehole extensometer records. Ground Water 42 (1), pp. 45-58.

Rashleigh, S.C. (1982). Fiber optic sensors operating at DC. U.S. Patent 4,495,411.

Sacks, I. S., Suyehiro, S., Evertson, D. W., and Yamagishi, Y. (1971). Sacks-evertson strainmeter, its installation in japan and some preliminary results concerning strain steps. Papers in Meteorology and Geophysics, 22, 195-207.

Schuite, J., L. Longuevergne, O. Bour, N. Guihéneuf, M. W. Becker, M. Cole, T. J. Burbey, N. Lavenant, and F. Boudin (2017), Combining periodic hydraulic tests and surface tilt measurements to explore in situ fracture hydromechanics, J. Geophys. Res. Solid Earth, 122, 6046–6066, doi:10.1002/2017JB014045.

Schweisinger, T., Svenson, E. J., and Murdoch, L. C. (2011). Hydromechanical behavior during constant-rate pumping tests in fractured gneiss. Hydrogeology Journal, 19, 963-980.

Streltsova, T.D. (1988), Well Testing in Heterogeneous Formations, 413 pp. New York, Chichester, Brisbane, Toronto, Singapore: John Wiley. ISBN 0 471 63169 8.

Sun, Y., Xue, Z., Hashimoto, T., Lei, X.,& Zhang, Y. (2020). Distributed Fiber Optic Sensing System for Well-Based Monitoring Water Injection Tests—A Geomechanical Response Perspective..Water Resources Research, 56,e2019WR024794. https://doi.org/10.1029/2019WR024794.

Svenson, E.J., Schweisinger, T., Murdoch, L.C., 2008. Field evaluation of the hydromechanical behavior of flat-lying fractures during slug tests. Journal of Hydrology 359, 30-45.

Teatini, P., L Tosi, T Strozzi, L Carbognin, U Wegmülle. 2005. Mapping regional land displacements in the Venice coastland by an integrated monitoring system. Remote Sensing of Environment, 98, 4. 403-413. 2005.

Vasco DW, Farr TG, Jeanne P, Doughty C, Nico P. Satellite-based monitoring of groundwater depletion in California's Central Valley. Sci Rep. 2019 Nov;9(1) 16053. doi:10.1038/s41598-019-52371-7. PMID: 31690776; PMCID: PMC6831828.

Vasco, D., Karaski, K., and Myer, L. (1998). Monitoring of fluid injection and soil consolidation using surface tilt measurements. Journal of Geotechnical and Geoenvironmental Engineering, 1124(1): 29-37.

Xue, Z. and T. Hashimoto. 2017. Geomechanical monitoring of caprock and wellbore integrity using fiber optic cable: strain measurement from the fluid injection and extraction field tests. Energy Procedia. V. 114, July. Pp. 3305-3011.

Yavuz, S. Barry Freifeld, Roman Pevzner, Aleksandar Dzunic, Sasha Ziramov, Andrej Bóna, Julia Correa, Konstantin Tertyshnikov, Milovan Urosevic, Michelle Robertson & Thomas Daley (2019) The initial appraisal of buried DAS system in CO2CRC Otway Project: the comparison of buried standard

633 fibre-optic and helically wound cables using 2D imaging, Exploration Geophysics, 50:1, 12-
634 21, DOI: 10.1080/08123985.2018.1561147.

635 Zhang, C. Cheng-Cheng, Bin Shi, Song Zhang, Kai Gu, Su-Ping Liu, Xu-Long Gong & Guang-Qing Wei.
636 2021. Microanchored borehole fiber optics allows strain profiling of the shallow subsurface.
637 Scientific Reports. (2021) 11:9173 | https://doi.org/10.1038/s41598-021-88526-8.

638 Zumberge, M. A., Berger, J., Dzieciuch, M. A., and Parker, R. L. (2004). Resolving Quadrature Fringes
639 in Real Time. Applied Optics, 43(4):771–775.

640

641

642

643

644

645

646